ADVANCING EARTH AND SPACE SCIENCE

JGR Space Physics

RESEARCH ARTICLE
10.1029/2020JA027993

Key Points:
- We robustly analyzed the 3-D structure of ionospheric anomalies immediately before and after the 2011 Tohoku-oki (M_w9.0) earthquake
- The preseismic anomalies consist of positive (~300 km height) and negative (~600 km height) anomalies over the land of NE Japan
- The postseismic electron depletion occurred offshore above the ruptured fault

Supporting Information:
- Supporting Information S1

Correspondence to:
I. N. Muafiry,
ihsanmuafiry@frontier.hokudai.ac.jp

Citation:
Muafiry, I. N., & Heki, K. (2020). 3-D tomography of the ionospheric anomalies immediately before and after the 2011 Tohoku-oki (M_w9.0) earthquake. *Journal of Geophysical Research: Space Physics*, *125*, e2020JA027993. https://doi.org/10.1029/2020JA027993

Received 16 MAR 2020
Accepted 6 AUG 2020
Accepted article online 31 AUG 2020

3-D Tomography of the Ionospheric Anomalies Immediately Before and After the 2011 Tohoku-Oki (M_w9.0) Earthquake

Ihsan Naufal Muafiry[1] **and Kosuke Heki**[1]

[1]Department Natural History Sciences, Hokkaido University, Sapporo, Japan

Abstract A dense network of ground global navigation satellite system receivers detected ionospheric total electron content (TEC) changes starting ~40 min before the 2011 Tohoku-oki (M_w9.0) earthquake around the ruptured fault, together with the long-lasting postseismic TEC drop. In this paper, we robustly estimate three-dimensional (3-D) distribution of both preseismic and postseismic ionospheric anomalies of the 2011 Tohoku-oki earthquake by tomographic inversions of electron density anomalies. We set up >6,000 blocks, as large as 1.0° (east-west) × 0.9° (north-south) × 60 km (vertical), over the Japanese Islands, the Sea of Japan, and the Korean Peninsula, up to 870 km altitude. By using TEC anomalies of pairs exceeding ~1,300 stations and eight satellites obtained using reference curves, we estimated electron density anomalies within individual blocks. The results showed that the preseismic and postseismic anomalies do not overlap in space. The preseismic anomalies are composed of low (~300 km height) positive and high (~600 km height) negative anomalies. They occurred above the land of NE Japan without extending offshore, suggesting its origin related to surface electric charges. On the other hand, the postseismic electron depletion occurred offshore above the region where large coseismic uplift took place. These results demonstrate that the preseismic and postseismic ionospheric anomalies are independent not only temporarily but also spatially and certainly in underlying physical mechanisms. We propose a simple model to explain how surface charges redistribute ionospheric electrons to make the observed preseismic electron density anomalies.

Plain Language Summary A dense network of GNSS/GPS receivers found that redistribution of ionospheric electrons started ~40 min before the 2011 Tohoku-oki earthquake around the fault. It was also found that a long-lasting electron depletion occurred after the earthquake. We studied the three-dimensional structures of the electron density anomalies immediately before and after the 2011 earthquake. We found that the preseismic anomaly occurred above land, but the postseismic anomaly occurred offshore. The preseismic change is characterized by the simultaneous growth of positive and negative electron density anomalies, while the postseismic change is dominated by an electron decrease. These differences reflect the different physical origins of the preseismic and postseismic anomalies.

1. Introduction: History of the Debate

Differential ionospheric delays (phase advances) of the two microwave carriers from GNSS satellites, such as the Global Positioning System (GPS), enable us to study ionospheric TEC and its change in high temporal and spatial resolutions. TEC data represent the number of electrons integrated along the line-of-sight (LoS) connecting satellites and ground receivers. Vertical crustal movements associated with large earthquakes trigger direct acoustic waves propagating upward. They reach the F-region of the ionosphere 8–10 min after earthquakes and disturb ionosphere causing changes in TEC.

Such a coseismic ionospheric disturbance (CID) has been first studied with GNSS by Calais and Minster (1995) and with a dense GNSS network by Heki and Ping (2005). Later, Astafyeva et al. (2011) studied immediate ionospheric response to the 2011 Tohoku-oki earthquake, and Rolland et al. (2013) clarified mechanisms of several important properties such as the CID directivity. Cahyadi and Heki (2015) proposed an empirical law connecting the earthquake magnitude and the CID amplitudes, and Astafyeva and Shults (2019) explored the way to study smaller earthquakes with CID. As reviewed in Heki (2020), the Japanese dense network GEONET (GNSS Earth Observation Network) produces TEC data with high

spatial (~20 km) and temporal (30 s) resolution and contributed to our understanding of ionospheric disturbances related to earthquakes.

Shortly after the 11 March 2011 Tohoku-oki (M_w9.0) earthquake, Heki (2011) reported the occurrence of positive (and partly negative) changes in TEC starting ~40 min before the earthquake near the epicenter using GEONET. Heki (2011) also reported the occurrences of similar anomalies before the 2004 Sumatra-Andaman (M_w9.2), 2010 Maule (M_w8.8), and the 1994 Hokkaido Toho-oki (M_w8.3) earthquakes.

Then three papers published after that (Kamogawa & Kakinami, 2013; Masci et al., 2015; Utada & Shimizu, 2014) doubted the reality of the TEC changes before the 2011 Tohoku-oki earthquake. Coseismic acoustic disturbance makes not only short-term N-shaped TEC changes but also airglow (Inchin et al., 2020) and long-lasting electron depletion in the ionosphere (Kakinami et al., 2012; Shinagawa et al., 2013; Zettergren & Snively, 2019). In Heki (2011), the TEC anomalies were defined as the departure from the reference curves. The major criticism by these three papers is that the enhancement is an artifact that emerged by using the data after the earthquake (including the long-lasting TEC drop) in defining the reference curves.

Rebuttals to these three papers have been published in the same journal (Heki & Enomoto, 2013, 2014, 2015). For example, Heki and Enomoto (2015) showed the reality of the positive bending of TEC before earthquakes using the Akaike information criterion (AIC). They confirmed statistical significance of the bending immediately before large earthquakes (e.g., 40 min before the 2011 Tohoku-oki earthquake), demonstrating that such bending could be detected even without using the data after earthquake occurrences. They further demonstrated that the leading times and the intensities of the bending depend on M_w from seven large earthquakes with reasonable amount of available GNSS data.

In a mean time, a new algorithm to detect such preseismic TEC changes was proposed by focusing the spatial correlation of preseismic TEC data (Iwata & Umeno, 2016). This work, together with Heki and Enomoto (2015), substantiates the existence of the preseismic anomalies. Subsequently, He and Heki (2017) lowered the threshold of earthquake magnitudes and compiled similar TEC enhancements prior to 18 earthquakes worldwide with M_w 7.3–9.2 and confirmed systematic M_w dependence of preseismic ionospheric anomalies, that is, the anomalies for earthquakes of larger M_w start earlier and grow stronger (relative to background TEC).

The physical mechanism responsible for these preseismic signals is only partly understood. Evidences obtained so far suggest it electromagnetic, assuming, for example, positive surface charges responsible for the ionospheric electron redistribution. Mobile positive holes generated by the breakage of the peroxy bonds that are ubiquitous in rocks (Freund, 2011) offer a scenario consistent with the TEC observations. The holes are a quantum mechanical state and spread as fast as a few hundreds of meters per second from seismogenic depths to the surface (Freund, 2013). Regarding the ionospheric electron redistribution by surface charges, several mechanisms have been proposed, for example, Kuo et al. (2014) and Kelley et al. (2017). This issue will be discussed in detail in section 5.

To understand the underlying physical process, it is effective to investigate the spatial structure and temporal evolution of the preseismic electron density anomalies. Recently, He and Heki (2018) studied the spatial structure of the electron density anomalies before the 2015 Illapel earthquake, Chile (M_w8.3), using 3-D tomography technique. The result suggested that the preseismic changes were composed of two parts, ionosphere electron density increase and decrease. They emerged ~20 min before earthquake and are situated at lower and higher altitudes, respectively, along the geomagnetic field. The same 3-D tomography technique has been applied for studies of 3-D structures of electron density changes by the 2017 total eclipse in North America (He et al., 2018) and sporadic-E irregularities in Japan (Muafiry et al., 2018).

In this study, we apply an improved version of the 3-D tomography technique to anomalies immediately before the 2011 Tohoku-oki earthquake. The anomaly signals are stronger than the 2015 Illapel earthquake and would help us better understand the 3-D structure and the evolution of the ionospheric electron density anomalies. The leading time of the preseismic anomaly of the 2011 earthquake is longer (~40 min) than the 2015 earthquake (~20 min). This makes us select the objective procedure to isolate the TEC anomalies carefully, and this issue will be discussed in section 2.

In sections 4 and 5, we compare the anomalies immediately before the 2011 Tohoku-oki and 2015 Illapel earthquakes and propose a simple mechanism to redistribute ionospheric electrons by surface charges. Subsequently, we study the 3-D structure of the postseismic TEC anomalies of the 2011 Tohoku-oki earthquake and discuss its difference from the preseismic anomalies. Then we demonstrate that the variety of signatures obtained immediately before and after large earthquakes originate from different combination of the penetrations of LoS with the preseismic and postseismic electron density anomalies.

2. Data Set and Methodology

2.1. VTEC From GNSS Data

We used GNSS data from the entire GEONET, a dense array of continuous GNSS receiving stations in Japan. We also add data from the GNSS network in South Korea, with 53 stations and ~40 km average separation (Choi & Hong, 2019), to reinforce the resolution in the western part of the studied area. In total, we used 1,284 GNSS stations to study both the preseismic and postseismic anomalies of the 2011 Tohoku-oki earthquake (Figure 1a). We used eight GPS satellites (PRN 05, 09, 15, 18, 21, 26, 27, and 28) visible from the studied region immediately before the mainshock (05:45 UT). Unfortunately, GEONET did not track GNSS other than GPS in 2011.

We converted the GNSS phase difference between the L1 (~1.5 GHz) and L2 (~1.2 GHz) carriers into slant TEC (STEC) and let them align with the differences of the pseudoranges of the two frequencies. Then we removed the satellite and receiver interfrequency biases made available by the Electric Navigation Research Institute (ENRI), Japan (Sakai, 2005), to isolate the absolute STEC, the number of electrons integrated along the LoS. They are converted to absolute vertical TEC (VTEC) by multiplying by the cosine of the incident angles of LoS with a thin layer at 300 km altitude. Figure 1b shows the distribution of LoS of the satellite-station pairs (8,533 pairs) used in the 3-D tomography calculation. For the Korean stations, we determined the receiver biases by minimum scalloping (Rideout & Coster, 2006).

2.2. Fitting Reference Curves to VTEC Time Series

After obtaining the VTEC time series, we model them using polynomials of time to extract preseismic signals. This method has been often criticized by two reasons: (1) Postseismic drops influence the reference curves and cause artificial enhancements, and (2) it is inappropriate to use the TEC data after the earthquake for earthquake prediction studies. As for (1), we avoid the influence of the postseismic drop by excluding the part of VTEC time series when SIP (subionospheric point, the ground projection of the intersection of LoS with a thin layer at 300 km altitude) is above the focal area (see Figure 2 inset maps). Considering the mechanism of postseismic TEC drops by downward plasma transport and recombination (Kakinami et al., 2012; Shinagawa et al., 2013) and numerical simulation of its long-term behavior (Zettergren & Snively, 2019), it is unlikely that the area of postseismic drop occurs in areas far from the focal area, and we can mostly avoid its influence by excluding VTEC data with SIP overlapping the focal region. This will be discussed again later in this section.

Regarding (2), this study does not aim at practical earthquake prediction by observing GNSS-TEC. We investigate ionospheric TEC behaviors immediately before and after large earthquakes by comparing with TEC well before and well after a series of earthquake-related disturbances. The reference curve method is appropriate to study preseismic and postseismic signals because earthquakes would not leave permanent changes (like coseismic steps in station coordinates) in TEC.

There are numbers of difference in the method to obtain the TEC anomalies from the early study (Heki, 2011). Here we explain the three main differences, (1) input data, (2) selection of exclusion windows, and (3) determination of polynomial degrees.

For point (1), we convert biased STEC to absolute VTEC beforehand and directly fit reference curves to the absolute VTEC time series. This is different from Heki (2011), where both polynomial coefficients and the bias are estimated simultaneously using STEC time series as the input data. The new method enables us to model the time series using higher-order polynomials and to optimize the polynomial degrees using the L-curve method. Another difference is that here we include the satellites that do not show significant anomalies. For example, GPS Sat.18 was not studied in Heki (2011) because they showed little TEC anomalies. However, such data are important to show where preseismic anomalies do “not” emerge. After all, we

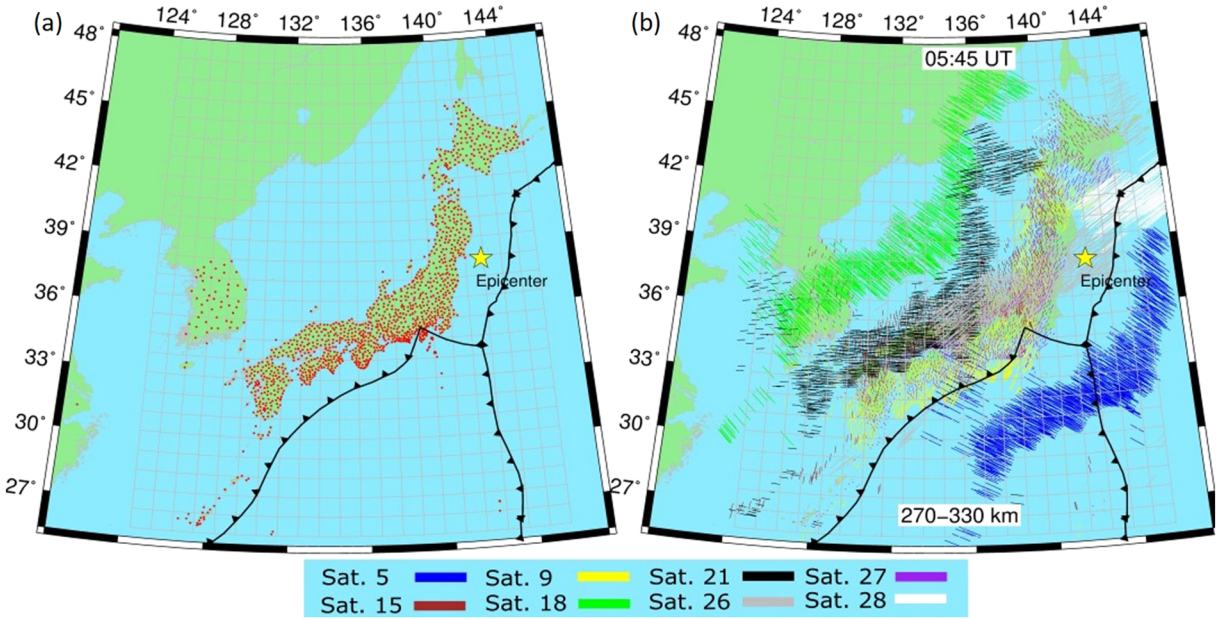

Figure 1. Maps showing the GNSS station distribution (red dots) and the voxels for 3-D tomography above Japan, the Sea of Japan, and the Eurasian Continent including the Korean Peninsula (a). Yellow star indicates the epicenter of the 2011 Tohoku-oki (M_W9.0) earthquake. Black curves illustrate boundaries between tectonic plates in and around the Japanese Islands. The short lines indicate the LoS of satellite-station pairs at the altitude 270–330 km 1 min before the earthquake (b). Color of the lines indicates satellite numbers.

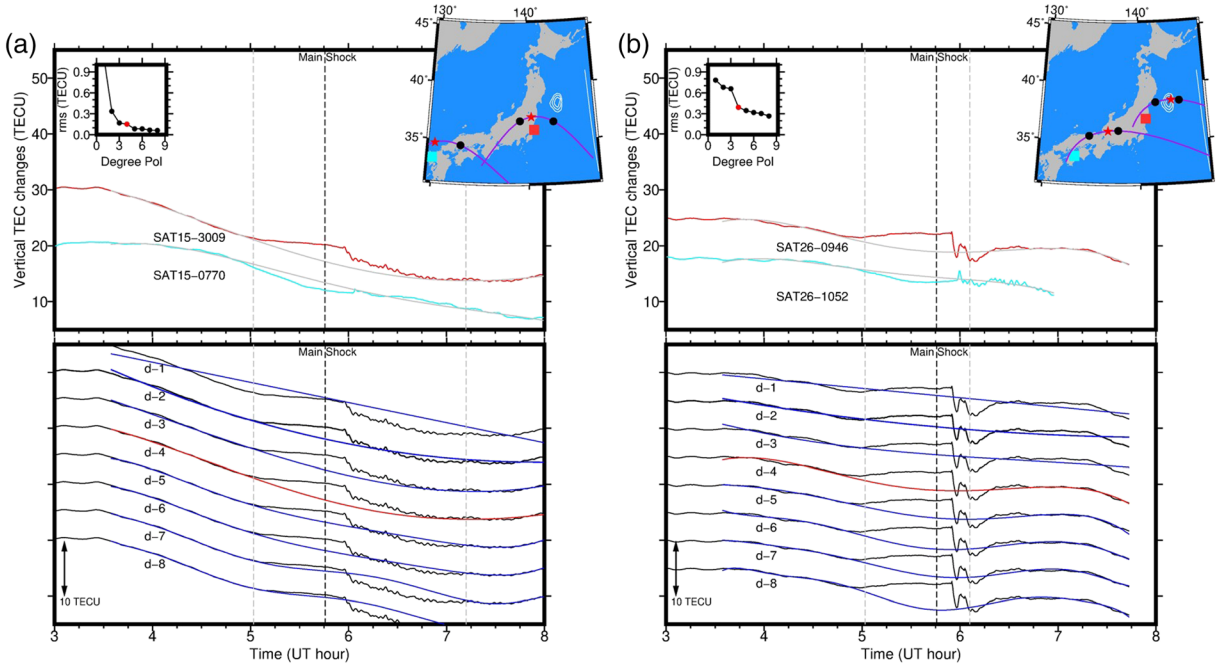

Figure 2. Fitting reference curves of VTEC changes for satellite-receiver pairs of GPS Sat.15-3009 (a) and Sat.26-0946 (b) showing positive preseismic anomalies (upper panel, red curves). We also show two different pairs showing negative anomalies for comparison (upper panel, cyan curves). Vertical dashed lines indicate the exclusion window in fitting the model with polynomials. Red stars and black circles attached to the SIP (subionospheric point) tracks in the inset maps show the SIP positions at the main shock and at the start and end of the exclusion window (we assumed 300 km to calculate the SIP positions). Red and cyan rectangles indicate the locations of the two receivers. The maps also include the coseismic slip distribution drawn with the contours of 3 m step (Ozawa et al., 2011). The L-curves in the left insets show the root mean square (rms) of the VTEC residuals obtained by fitting curves of various polynomial degrees. We employed the red curves in the lower panels, that is, degree 4 for (a) and (b), that showed significant rms drops in the L-curves.

used eight GPS satellites including four new satellites 5, 18, 21, and 28 in addition to 9, 15, 26, and 27 studied in Heki (2011). Samples of the time series of these new satellites are given in the supporting information Figure S1.

Regarding point (2), Heki (2011) excluded a time window 5.2–6.0 UT possibly influenced by the preseismic, coseismic, and postseismic ionospheric disturbances in fitting the reference curves for all the four satellites. Here, we fit the polynomial to absolute VTEC using the excluding windows whose start and end times are determined from external information. The selection of the end of this exclusion window is especially important because reference curves estimated using the period influenced by the long-lasting postseismic TEC drop may give rise to artificial preseismic TEC increase. Actually, in Figure S2, we demonstrate that the VTEC anomalies during the preseismic period 5:05–5:46 UT is not so sensitive to the excluding window settings using the case of Figure 2a.

For the start of the exclusion window, we employed the onset of the preseismic anomaly 5:05 UT for all the satellites (~40 min prior to the main shock). This time was obtained by Heki and Enomoto (2015) by searching significant positive bending in VTEC time series using AIC. As shown in Figure S2a, changing this starting time by ±12 min does not make significant differences in the reference curves for this pair of the satellite and the station.

Regarding the end time of the exclusion window, we assume that the postseismic drop occurs by coseismic vertical crustal movement and hence over the ruptured fault. This will be confirmed later in section 4 and supported by a numerical simulation, for example, Figure 4a of Zettergren and Snively (2019). We determined the end time of the exclusion window by drawing the SIP trajectories to know the time for SIP to go out of the affected area (defined as the area above the fault with slips exceeding 3 m). Naturally, the end times depend on satellites (see Figure 2 inset maps). Table S1 lists the exclusion time windows for individual satellites used in this study (windows depend on regions of the stations, too, for some satellites). It should be noted that we do not rely on the decay of the hole, which may last for hours, but avoid the spatial overlap of the hole with the LoS. This procedure enables us to isolate the VTEC anomalies caused by the earthquake robustly to a certain extent. Using the Figure 2a case, Figure S2b demonstrates that moving the ending time of the exclusion window by 24 min backward and forward let positive anomalies immediately before the earthquake change by only −3.7% and +10.8%, respectively. This suggests that the uncertainty in the ending time of a few tens of minutes is not crucial in isolating the preseismic VTEC anomalies.

For the satellites whose SIP does not go over the focal area (e.g., Sat.18), we fixed the end of the excluding window at 10 min after the earthquake. For a few satellites (e.g., Sat.5 and Sat.28) with short postseismic VTEC data, we had to set up earlier end times for a part of stations (e.g., 5 min after the earthquake). We did not set up a specific elevation cut-off angle and assumed a thin layer at 300 km for STEC-VTEC conversion regardless of the elevations.

As for the point (3), we used the L-curve method to determine the optimum degree of polynomials curve (see Figure 7 of He & Heki, 2017). We calculate root mean squares (rms) using the postfit residuals outside the exclusion windows. Their dependence on the polynomial degree is shown in the left insets of Figure 2. We considered that the lower-left edge of the L-curve provides the most appropriate degree of polynomial to fit the VTEC changes. Table S1 also shows the degrees of polynomials for different satellites we employed. In Figure 2, we use the total time span of 5 hr for satellites 15 and 26 (the time spans are shorter for other satellites). The time spans also influence the best polynomial degree, that is, the best degree tends to be higher for a longer time span. However, the shapes of the anomalies within the exclusion windows are not much influenced by the total time spans.

We used the departure from these reference curves (TEC anomalies) as the input for our 3-D tomography calculation. In doing so, we converted the VTEC anomalies back to the STEC anomalies by dividing with cosine of the incidence angle of LoS to the 300 km layer. In short, we took advantage of VTEC for its simplicity in fitting the reference curves (because the apparent changes caused by elevation angle variations are already removed). However, we used the values after converting to STEC anomalies for 3-D tomography.

As emphasized in Heki and Enomoto (2013) and He and Heki (2016), preseismic TEC anomalies take either positive or negative values. In Figure 2, we show examples of VTEC time series showing positive and negative preseismic TEC anomalies with red and cyan curves, respectively. The difference would originate from

the difference of the parts in ionosphere these LoS penetrate, that is, the former would have penetrated more positive parts than negative parts of the electron density anomalies, and vice versa. The purpose of the present study is to understand how such differences occur.

2.3. Set-Up of Voxels for 3-D Tomography

For the 3-D tomography, we set up ~6,800 blocks over the Japanese Islands, the Sea of Japan, and the Korean Peninsula, with the size of 1.0° (east-west) × 0.9° (north-south) × 60 km (vertical) for altitudes 90–870 km (Figure 1). The electron density within a block was assumed to be homogeneous. One LoS penetrates multiple blocks, and the STEC residual for that LoS can be expressed as the sum of the products of the penetration lengths and electron density anomalies of the penetrated blocks. We calculated the penetration length as the distance between the two intersections of LoS with the block surface by simple geometric calculations. For the calculation, we considered that the Earth is a sphere (i.e., its ellipticity is neglected) with an average radius.

Although the LoS are densely distributed, they do not penetrate all the blocks, especially above the oceanic areas. Hence, we need to introduce certain constraints to regularize the least squares inversion. Here, we applied a continuity constraint, that is, we assumed that neighboring blocks have the same electron density anomalies with a certain allowance for the difference. We assumed 0.10×10^{11} el/m^3 as the allowance. We assumed the uniform STEC observation errors of 0.2 TECU (1 TECU is 10^{16} el/m^2). This is a few times as large as the typical error for differential GNSS VTEC measurements (Coster et al., 2013) but was consistent with the post-fit STEC residuals in our previous studies (He et al., 2018; He & Heki, 2018; Muafiry et al., 2018).

As an additional constraint, we weakly constrained the electron density anomalies around zero with an altitude-dependent allowance. According to the Chapman distribution, electron density at height h is proportional to $\exp(1 - A - e^{-A})/2$, where A equals $(h - h_{max})/H$. There h_{max} is the electron density peak altitude (300 km) and H is assumed 80 km. This distribution matches with the profiles measured by radio occultation above NE Japan during the studied period and calculated using the International Reference Ionosphere (IRI) 2007 model, as illustrated in Astafyeva et al. (2011). We made the allowance proportional to this distribution (1% of the electron density at that altitude), that is, we constrained the electron density around zero strongly for altitudes in the D and E regions and weakly in the F region of the ionosphere. This is to avoid estimation of unrealistically large electron density anomalies in very high or very low altitudes (influence of this constraint on the results is shown in Figure S4). Applying these constraints, we performed linear least squares estimation of electron density anomalies for all the blocks, first using synthetic data and then using the real data.

3. Resolution Tests

The accuracy of the 3-D tomography can be assessed by performing the inversion to recover artificial distribution of electron density anomalies using synthetic data. We first perform such a resolution test with the classical checkerboard pattern. We assumed the same satellite and station geometry as the epoch 05:45 UT, 1 min before the earthquake, to synthesize the input STEC data for the 3-D tomography. In recovering the 3-D distribution of electron density anomalies, we applied the constraints explained in the previous chapter.

Figure 3a shows the assumed checkerboard pattern. It is composed of the electron density anomalies of $\pm 2.00 \times 10^{11}$ el/m^3. We let the anomaly change gradually between the positive and negative parts to make the pattern consistent with the continuity constraint. We also assumed the amplitudes of the anomalies to decay in very high and low ionosphere to make it compatible with the other constraint.

Figure 3b shows the recovered pattern for the blocks at the altitude range 270–330 km. The pattern is well recovered particularly over the land (i.e., the Japanese Islands) and the offshore area within ~200 km from the coast, including the area above the rupture. Similarly, in the vertical section the resolution remains good in the altitudes 150–510 km, although the amplitudes of the recovered anomalies are ~2/3 of the input model possibly originating from the constraint around zero. On the other hand, resolution is poor where we do not have enough LoS penetrations (Figure 1b). Such regions include the Pacific Ocean to the south of the rupture and the region above North Korea and Russia. The checkerboard test generally shows a high performance of

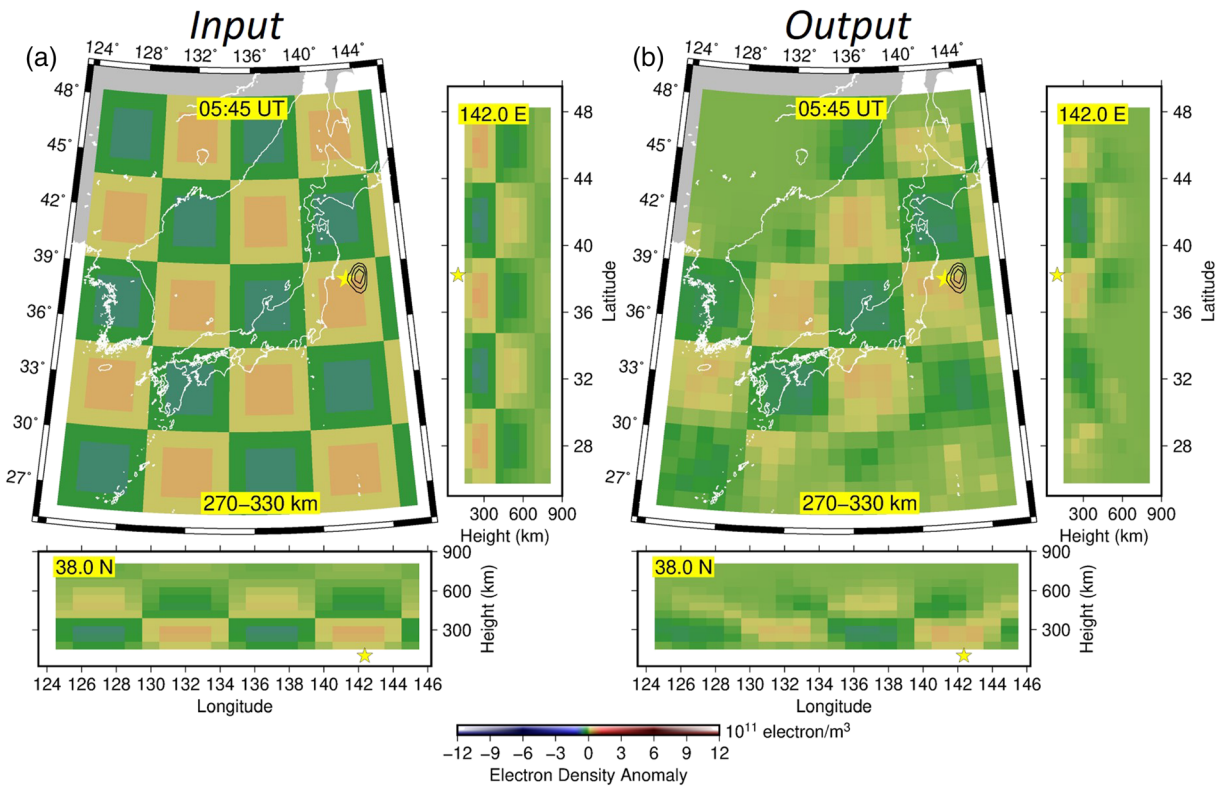

Figure 3. The resolution test with the classical checkerboard pattern. The assumed electron density anomalies (a) and the output of the 3-D tomography (b) are given in map view and north-south, east-west profiles.

our 3-D tomography in the region of interest. As suggested by Figure S6, vertical resolution is poor even above NE Japan for the highest layers of the blocks.

We next assessed the robustness of our result for later discussions on preseismic electron density anomalies, by recovering patterns composed of a pair of positive and negative ($\pm 3.00 \times 10^{11}$ el/m^3) anomalies in low and high altitudes, respectively, in neutral background (Figure 4a). The results (Figure 4b) well reproduced the assumed pattern of the positive anomaly again reduced to ~2/3 amplitude of the input model due to the constraints. Similarly, the positive and negative anomaly patterns in the latitudinal profiles are well recovered with only weak smears in surrounding blocks not exceeding a few percent of the assumed anomaly. The results of the two resolution tests show that our 3-D tomography results are accurate enough in the region of interest, where the TEC anomalies appeared immediately before and after the 2011 Tohoku-oki earthquake.

4. Tomography Results

4.1. Preseismic Anomalies

Figure 5 shows the map view of our 3-D tomography result for altitudes of 90–870 km at 05:45 UT, 1 min before the 2011 Tohoku-oki earthquake, with longitudinal and latitudinal profiles. In Figure S3 we show the results at five epochs before the earthquake (40, 30, 20, 10, and 1 min before the earthquake). We confirmed beforehand that the performance of the tomography remains high for all these epochs. The results present that the strong positive electron density anomalies occurred at 270–330 km and 330–390 km altitude layers and the anomalies grow large without notable pattern change or spatial drifts toward the main shock. In fact, the latitude of the voxel showing the largest positive anomaly stays around 38°N during the 40 min period.

An important feature is that the positive anomaly lies above the land of NE Japan rather than right above the focal area. Its implication will be discussed later. The longitudinal and latitudinal profiles

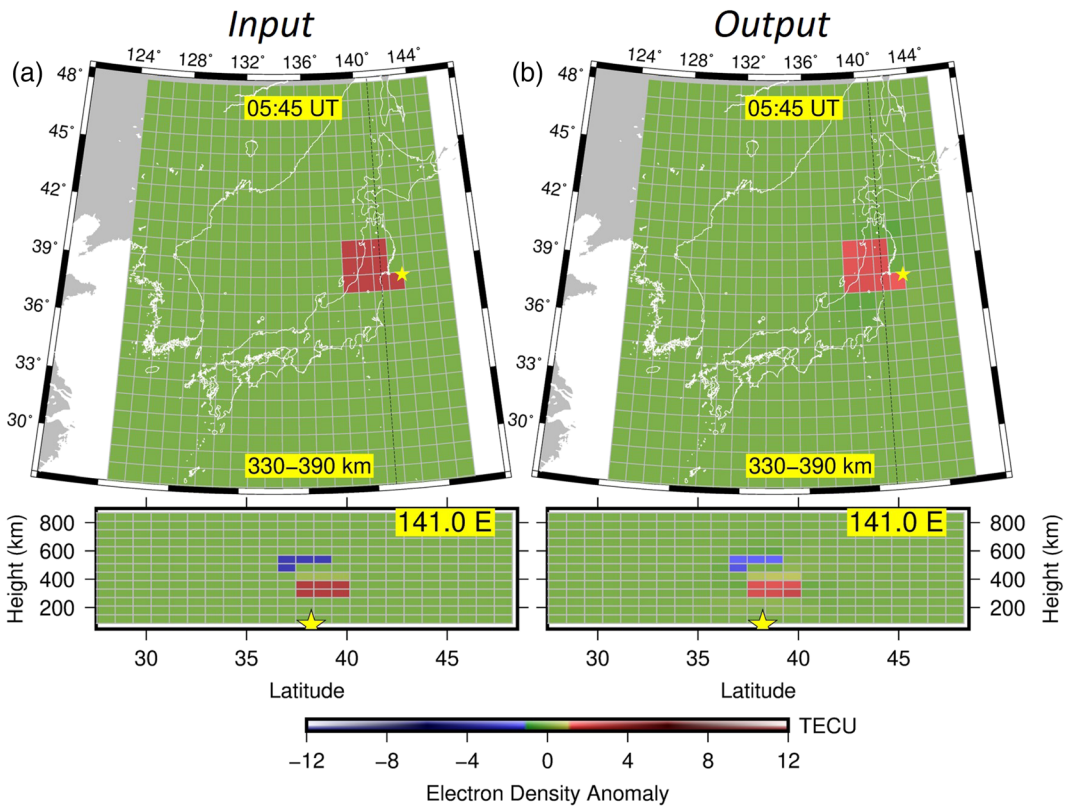

Figure 4. Second resolution test for a pair of compact positive and negative anomalies above NE Japan. The upper and bottom panels are horizontal view and latitudinal profile of the anomalies of the assumed pattern (a) and the output of the 3D tomography (b).

(Figures 5b and 5c) show that the positive anomaly is the strongest at altitude 270–390 km. Above this positive anomaly lies the negative anomaly at altitude ~600 km. These two anomalies are diffuse, and it is not very clear if they lie along the geomagnetic field. Nevertheless, the pattern resembles to the earlier report for the 3-D structure of the preseismic anomalies of the 2015 Illapel earthquake (He & Heki, 2018), a pair of positive (height 150–225 km) and negative (height 450–525 km) anomalies located along the geomagnetic field.

Figure 6 compares the observed and calculated anomalies for four satellites, 15, 18, 26, and 27, at the epoch 1 min before the main shock. The "observed" anomalies (Figure 6a) are those obtained as the departure from the reference curves to VTEC time series, and we plotted them at their SIP. On the other hand, the "calculated" anomalies (Figure 6b) were derived as the sum of the products of the estimated electron density anomalies (Figure 5) and the penetration lengths of voxels along the LoS. Such calculated STEC anomalies are converted to VTEC for comparison with the observed anomalies.

These two are expected to nearly coincide if the 3-D tomography inversion is successful. We can see that the observed TEC anomalies are well reproduced by the estimated 3-D electron density anomalies shown in Figure 5. Figure S5 provides two more assessments of the accuracy of the 3-D tomography, that is, reduction of the rms, and validation by confirming the coincidence of the randomly extracted subset of the input TEC anomaly data and those calculated using the 3-D electron density anomalies estimated without using the extracted subset.

Figure S4 compares the tomography results based on three different settings of the constraint around zero, that is, 1%, 3%, and 10% of the Chapman distribution. We see that the positive anomaly ~300 km high and negative anomaly ~600 km high persistently appear for those solutions. At the same time, a weaker constraint tends to yield complicated patterns in layers near the top of the blocks. As seen in Figure S6, LoS penetrate these high-altitude blocks almost vertically, suggesting poor vertical resolution of the recovered

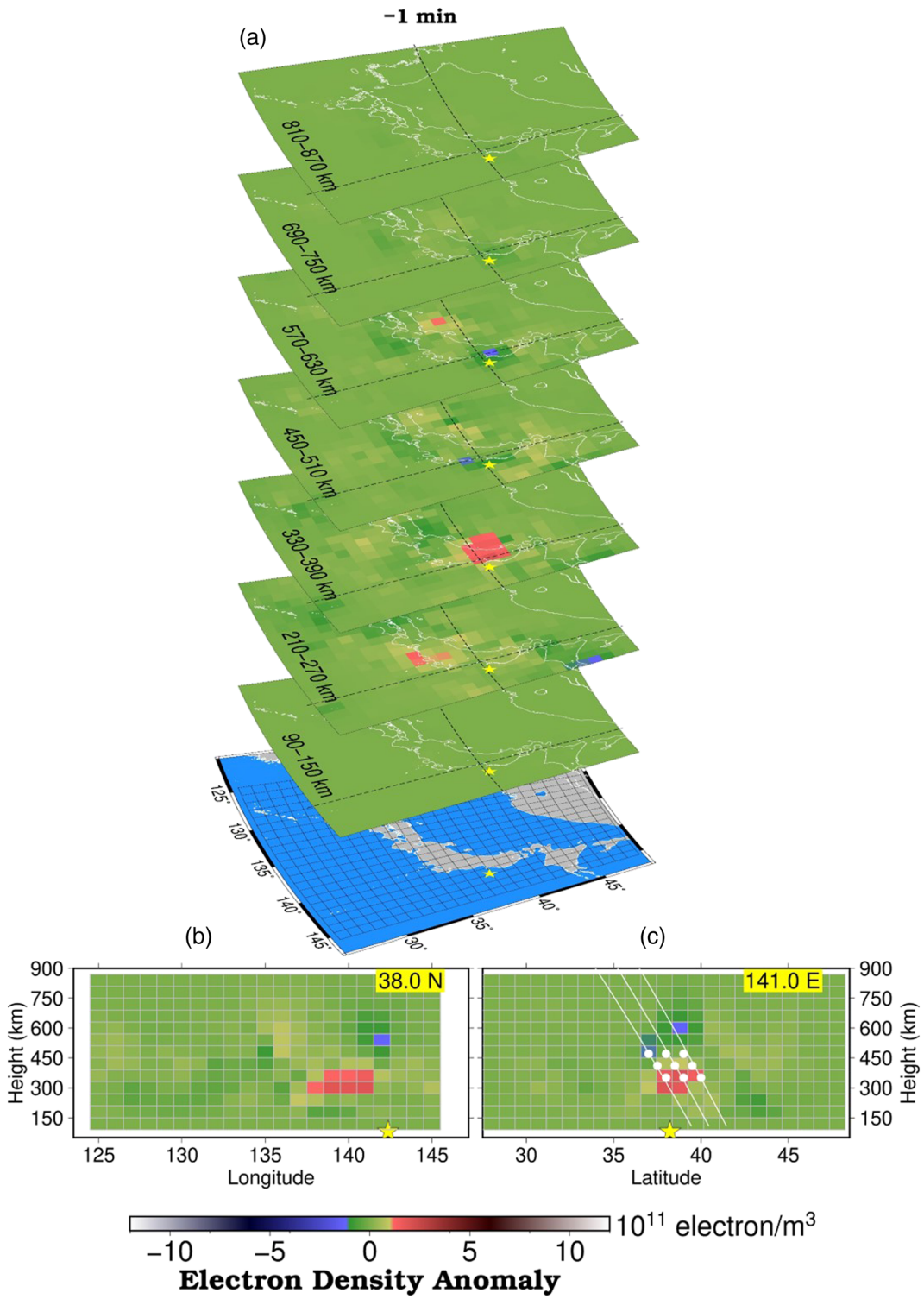

Figure 5. 3-D tomography results of electron density anomalies 1 min before the Tohoku-oki earthquake (a). We also show the east-west (b) and north-south (c) profiles. The white curves in (c) show the geomagnetic fields, and yellow stars show the latitude and longitude of the epicenter. White circles in (c) show selected positions used to draw Figure 7, and white lines in (c) show geomagnetic fields. The results for other epochs are given in Figure S3.

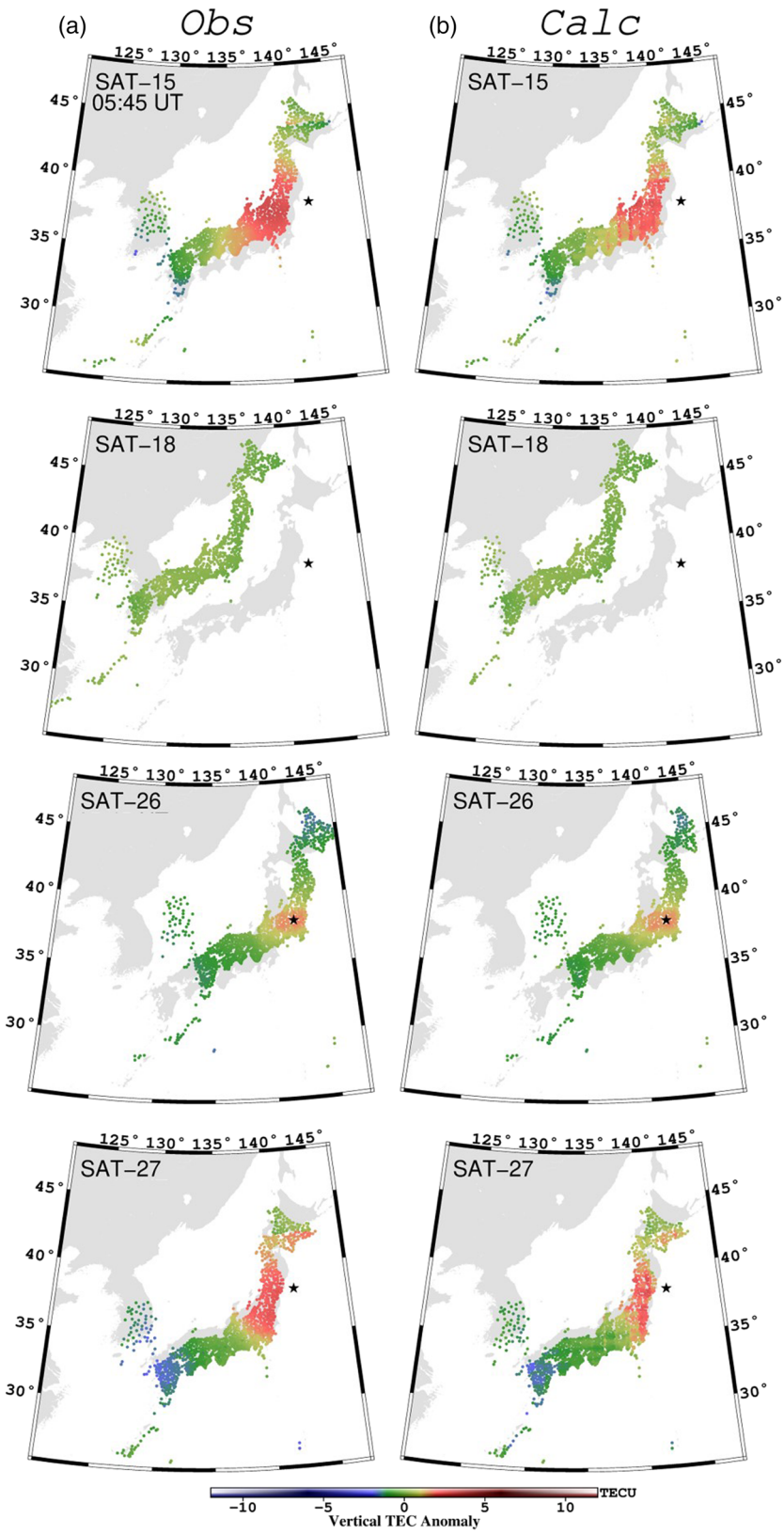

Figure 6. Comparison of the observed (a) and calculated (b) VTEC anomalies four GPS satellites at the epoch at 05:45 UT, 1 min before the earthquake. They are mostly consistent with each other showing that the estimated 3-D electron density anomaly structure well explains the observed TEC changes.

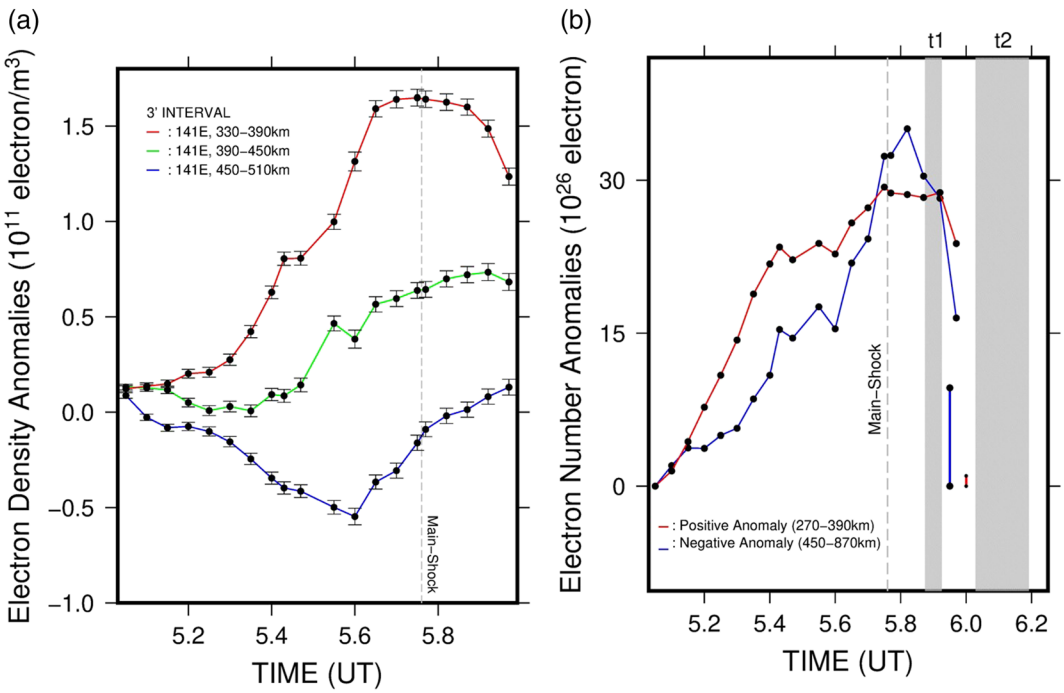

Figure 7. (a) The evolution of the average estimated electron density anomalies of the three different blocks at the three altitudes, 360, 420, 480 km (see Figure 5c for positions), with 3-min interval. The error bars are the average of the formal errors of the three voxels sampled at the three altitudes. Panel (b) shows the integrated amount of positive and negative anomalies at lower (270–390 km) and higher (450–870 km) altitude voxels, respectively. To the right side of (b), we show the spatially integrated increase in negative (blue) and positive (red) postseismic electron density anomalies measured as the difference between the two periods shown in gray squares (see Figure 9).

electron density anomalies under the given station and satellite distribution. We think that such irregular anomalies emerging in the highest layers for weak constraint cases are not real.

4.2. Growth and Polarity Balances of Preseismic Anomalies

To further study the evolution of the electron density anomalies immediately before the earthquake, in Figure 7a we plot the electron density anomalies at points with three different altitudes, 330–390 km, 390–450 km, and 450–510 km (white circles in Figure 5c) along the geomagnetic field. The three altitudes correspond to the center of positive anomaly, middle point between the positive and negative anomalies, and the center of negative anomaly, respectively. Figure 7a shows the averages of three blocks at low, medium, and high altitudes every 3 min before and after the earthquake. The positive anomalies show larger values than negative anomalies. However, this does not necessarily mean the dominance of the spatially integrated positive anomalies. Figure 7b indicates the total amount of positive and negative electron density anomalies obtained by integrating them in space. They are well balanced, suggesting that the growth of the anomalies occurred as the electron transport rather than net increase or decrease of electrons.

The build-up of the positive and negative anomalies starts ~40 min before the earthquake. They grow until ~20 min before the main shock and remain nearly constant until the earthquake. After the earthquake, the anomalies are stationary for ~10 min and start to decay. We have no idea on the fluctuations of the curve around 5.4–5.6 UT and sudden increase of the negative anomaly after 5.6 UT in Figure 7b. They may reflect a certain instability coming from the VTEC observation errors. It should be noted that we did not perform in our tomography any temporal smoothing which would be an effective remedy to reduce such instability.

4.3. Comparison With the 2015 Illapel Earthquake

Now we have examples of the 3-D distributions of ionospheric electron density anomalies immediately before two large earthquakes, that is, 2011 Tohoku-oki (M_w9.0, this study) and 2015 Illapel earthquake, central Chile (M_w8.3, He & Heki, 2018). They are compared in Figure 8. At a glance, we could see their

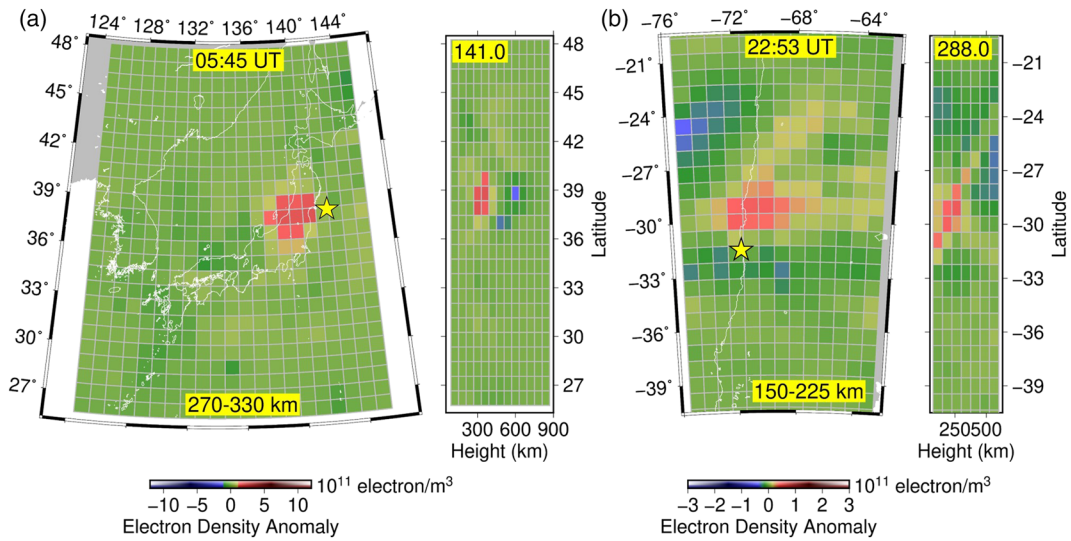

Figure 8. The estimated 3-D distributions of ionospheric electron density anomalies prior to the 2011 Tohoku-oki earthquake (this study) (a), and the 2015 Illapel earthquake (He & Heki, 2018) (b) drawn in the same spatial scale. Each case is composed of two panels showing the plan view and north-south profile at the longitude crossing the anomaly. Panels (a) and (b) use different color palettes, and the anomalies in (a) are ~7 times as strong as in (b). The yellow stars are the epicenters of the two events.

similarities. They are composed of low-altitude positive anomalies and high-altitude negative anomalies. However, they differ in the intensity of the anomaly (the two cases are drawn with different color palettes), that is, the positive anomalies of the 2011 Tohoku-oki are ~7 times as strong as those of the 2015 earthquake. Such a M_w dependence is also seen in the leading times and the intensities of the initial bending of the VTEC curves (He & Heki, 2017; Heki & Enomoto, 2015).

Their vertical profiles suggest that the altitudes of the positive and negative anomalies before the 2011 earthquake (~300 and ~600 km) are somewhat higher than the 2015 earthquake (~200 and ~500 km). On the other hand, horizontal extents of the anomalies are little different in the two cases, that is, the positive anomalies lie within circles with diameter of ~300 km. Here we emphasize that the strong positive anomalies do not occur directly above the epicenters but emerge only above land. This suggests that the electron redistribution is due to electric fields made by surface electric charges. Such surface charges would be relatively stable on land, but they diffuse rapidly in the ocean due to high electric conductivity of sea water (areal density of the surface charges would be determined by the balance between the production at depth and the diffusion at the surface). Horizontal extent of the anomaly before the 2011 Tohoku-oki earthquake might have been limited by the land-sea distribution in the Japanese Islands, that is, the anomaly may have expanded larger if the whole area is subaerial.

4.4. Postseismic Anomalies

Ionospheric electron density drops (formation of the tsunami hole) occurred following the arrival of acoustic waves at the ionospheric F region ~10 min after the 2011 Tohoku-oki earthquake (Kakinami et al., 2012; Shinagawa et al., 2013; Zettergren & Snively, 2019). Here we estimate the 3-D structure of this postseismic anomaly to study its difference from the preseismic anomalies.

At first, we get the medians of VTEC from the two periods, that is, 5:52–5:55 UT and 6:03–6:11 UT, in VTEC time series of GNSS stations (gray rectangles in Figure 9a). These periods correspond to times immediately before and after the ionospheric hole formation associated with the acoustic disturbance arrival. We do not use reference curves because the two periods are separated from each other by only ~10 min. The long-term TEC decrease due to the increasing solar zenith angle would appear as a negative bias of the whole region and not as a localized anomaly. We use the same eight satellites as the preseismic anomaly studies. We converted the difference of VTEC between the two epochs into STEC and used them as the input to our tomography program. We used the satellite positions at 6:00 UT, the time in the middle of the two periods (LoS

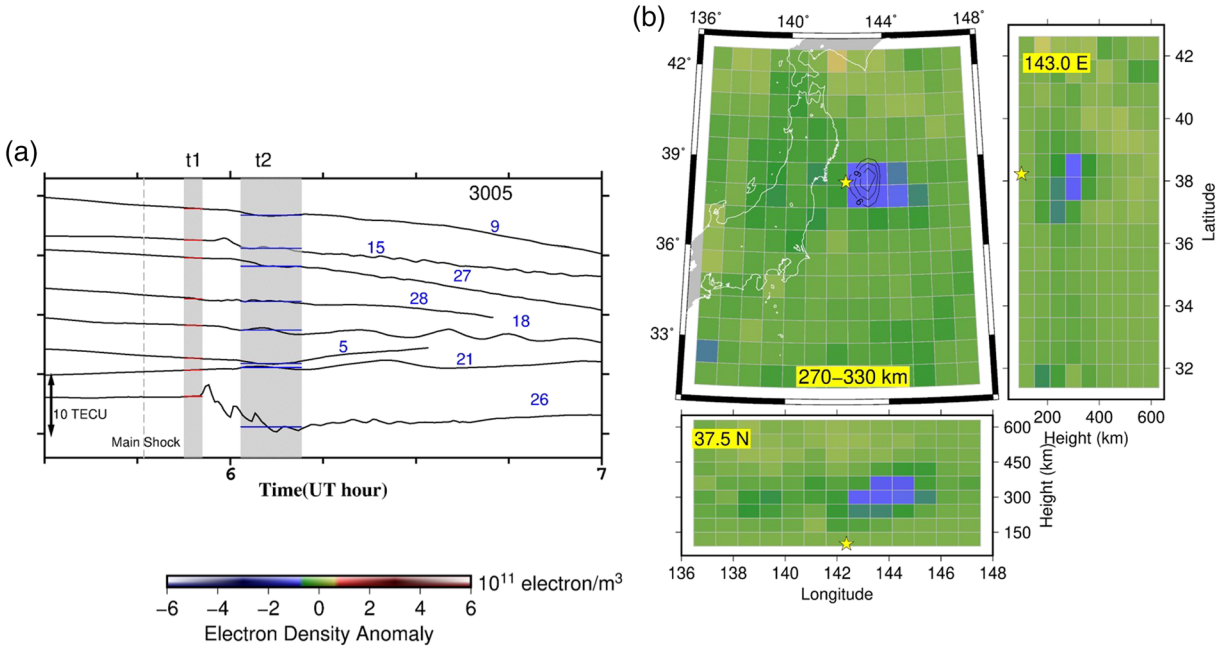

Figure 9. (a) VTEC time series of eight GPS satellites, observed at 3005 in Kanto. The VTEC drops are defined as the difference between the median VTEC values in the two periods (gray rectangles). The flat red and blue lines within the two periods indicate the VTEC medians in the two periods, and we used their differences as the input to the 3-D tomography. (b) 3-D tomography of the electron depletion induced by the coseismic uplift and subsequent drop of the sea surface after the 2011 Tohoku-oki earthquake (yellow stars represent the epicenter). The contours in the plan view show the fault slips in the main shock (the contour interval is 3 m). Spatially integrated amounts of negative and positive electron number changes are shown in Figure 7b.

movements during the 10 min period is much less than the voxel size). We applied the same constraints as in the preseismic case to regularize the inversion. We performed the resolution test similar to Figure 4 for the postseismic anomaly and show the results in Figure S7.

Figure 9b shows the 3-D structure of the recovered electron density anomalies associated with the formation of the postseismic ionospheric hole. An important point is that they occur offshore just above the area of large coseismic slips (contours in Figure 9b), in contrast to the preseismic anomalies that occurred above land (Figure 8a). The negative anomaly extends beyond the large slip region as far as ~145°E, but this would be the smearing as seen in the resolution test (Figure S4). Another important point is that the anomalies are mainly composed of negative changes (the amounts of positive and negative changes are compared in Figure 7b). These contrasts would reflect the different physical mechanisms responsible for the preseismic and postseismic anomalies, that is, the former is caused by electron transport, but the latter is caused by the recombination of the electrons displaced downward by the acoustic disturbance as modeled by Kakinami et al. (2012) and Shinagawa et al. (2013). We also see that the dimension of the hole is consistent with the numerical simulation by Zettergren and Snively (2019), although their assumption on the excitation source is simple. A more realistic simulation studies in the future would contribute to our understanding on the postseismic formation of the hole.

Now we identified three electron density anomalies different in time and polarity, that is, #1 the preseismic positive anomaly, #2 the preseismic negative anomaly, and #3 the postseismic negative anomaly. #1 and #2 start to grow simultaneously at low and high ionosphere ~40 min before the earthquake and decay after the earthquake, while #3 emerges shortly after the acoustic disturbance arriving 8–10 min after the earthquake and last for tens of minutes.

Heki (2011) noticed diversity of signatures of TEC disturbances related to earthquakes. For example, some LoS show only gradual growth and decay of positive signals (e.g., Sat.15-3009 shown in Figure 2a) while other LoS show sudden decrease after the acoustic disturbances (e.g. Sat.26-0946 shown in Figure 2b). On the other hand, some LoS, like the cyan time series in Figure 2 top, show negative changes during the pre-seismic period. These varieties reflect the difference in the penetration of those LoS with the anomalies #1,

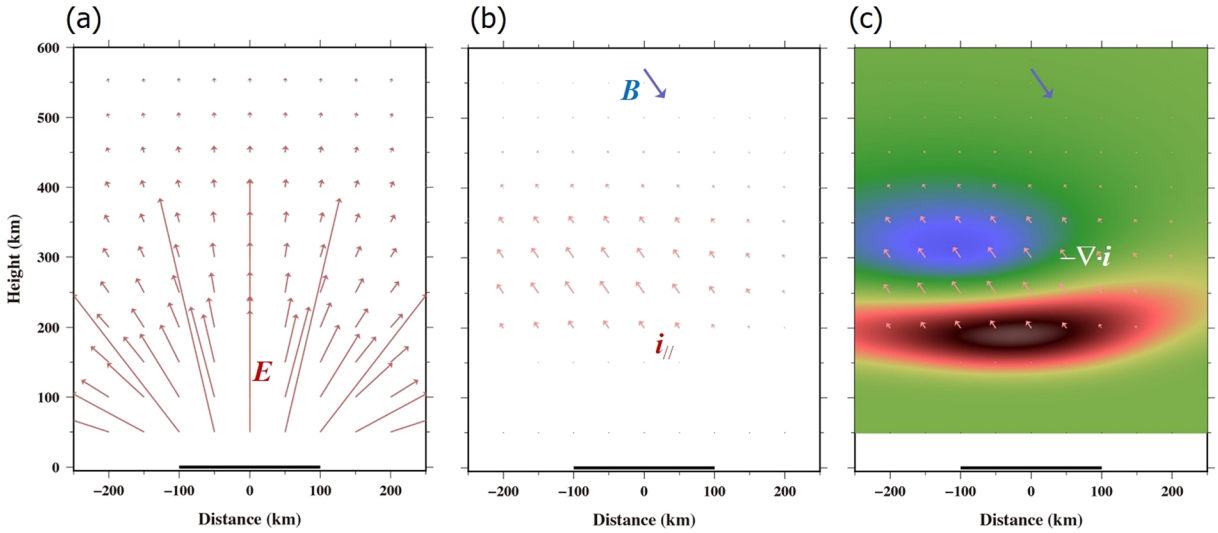

Figure 10. A two-dimensional image of the preseismic electron redistribution by surface electric charges. (a) Positive charges distributed on the surface (gray line at the bottom) make upward electric field $\boldsymbol{E}$, and (b) the component parallel with the geomagnetic field $\boldsymbol{B}$ exerts electromotive forces and drives electric current $\boldsymbol{i}_{//}$ along the geomagnetic field where there are enough free electrons. (c) Convergence and divergence of the electron flow make positive (red) and negative (blue) electron density anomalies, respectively. This is a qualitative model, and we do not give scales to convert the illustrated quantities to real values.

#2, and #3. For example, Sat.15-3009 penetrated only #1, while Sat.26-0946 penetrated both #2 and #3. Figure S8 explains the variety of waveforms of VTEC changes before and after the earthquake coming from the diversity in the penetrations of LoS with these three anomalies.

5. Discussion on Physical Mechanisms of Preseismic Anomalies

Our result showed that the total amounts of the positive and negative electron density anomalies increased in a similar manner (Figure 7b) suggesting little changes in the total number of electrons in the preseismic stage. Hence, such changes would have occurred without net increase or decrease of electrons, for example, by electron transportation, rather than enhanced ionization or recombination. Here we discuss possible physical mechanisms connecting the surface electric charges to the preseismic ionospheric electron redistributions.

Two hypotheses have been proposed to explain how surface electric charges redistribute ionospheric electrons. Kuo et al. (2014) showed that the anomaly can be generated by an upward electric current from stressed rock. This leads to the westward Hall electric field $\boldsymbol{E}$. This $\boldsymbol{E}$, together with the geomagnetic field $\boldsymbol{B}$, drives downward $\boldsymbol{E}\times\boldsymbol{B}$ drift of the ionospheric plasma and makes a pair of positive and negative electron density anomalies. This model, however, needs large electric fields near ground to let substantial electric current flow through the highly resistive lower atmosphere. Kelley et al. (2017) proposed that the $\boldsymbol{E}\times\boldsymbol{B}$ drift could be driven directly by electric fields made by surface electric charges. Their model needs the surface electric fields only ~1/500 of the fair-weather field to produce the anomalies observed before the 2011 Tohoku-oki earthquake.

Here we propose a new model focusing on the induced polarization that would occur together with the process proposed by Kelley et al. (2017). Figure 10 qualitatively illustrates the idea. Electric fields $\boldsymbol{E}$ made by surface charges would reach the ionosphere (Figure 10a). The field generates electromotive forces and makes electrons move along geomagnetic fields. If surface charges are positive, electron movements will be downward, and the current will be upward ($\boldsymbol{i}_{//}$ in Figure 10b). The current will continue until the induced electric field cancels the external field made by surface charges, making the electric potential uniform along the magnetic field. The current will depend on the along-$\boldsymbol{B}$ component of the external electric field and the density of free electrons as a function of altitude. The nonuniform electric currents would result in convergence/divergence of electrons and make positive/negative electron density anomalies at the lower/higher ionosphere along the magnetic field (Figure 10c), the structure we found in Chile (He & Heki, 2018) and in Japan (this study) by the 3-D tomography.

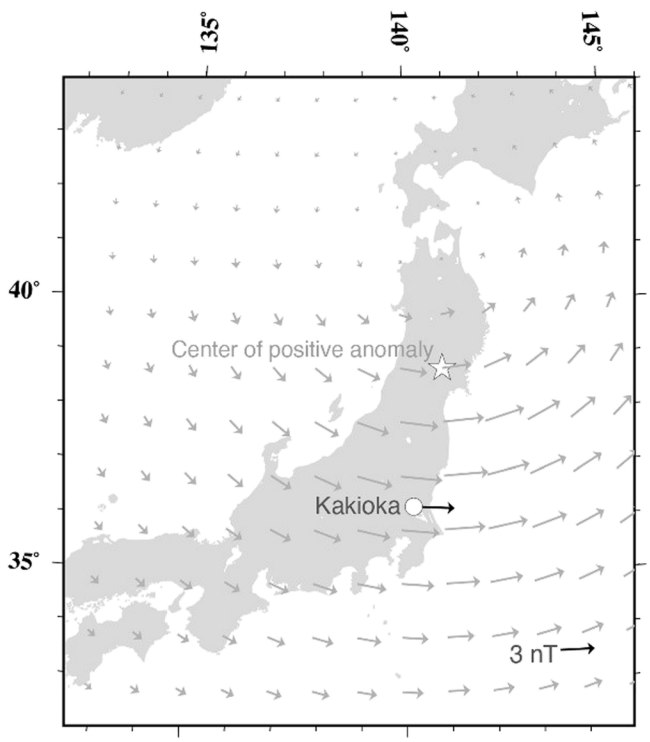

Figure 11. Magnetic field on the surface caused by the upward current along geomagnetic field above the star (center of positive anomaly), equivalent to cause ~0.15 of electron transport given in Figure 7b from altitude 330 to 600 km. This makes disturbing field of ~3 nT eastward at the Kakioka station, consistent with those reported in Heki and Enomoto (2013).

The model is qualitative, and we do not have actual figures for quantities such as areal density of surface charges and $\boldsymbol{E}$. This stems from the limitation of the GNSS-TEC method, that is, GNSS can sense only electrons and cannot count positive ions. In fact, substantial amount of positive ion would move together with electrons to keep the plasma "nearly" neutral (there should be deviation from neutral to cancel the external electric fields by the induced fields). In short, the 3-D tomography results do not allow us to directly infer $\boldsymbol{E}$ or $\boldsymbol{i}_{//}$.

One external test of the model might come from the magnetic fields possibly generated by the upward current along $\boldsymbol{B}$ ($\boldsymbol{i}_{//}$ in Figure 10b). Such a current would make eastward magnetic fields on surface, mainly in the region to the south of the epicenter (Figure 11). As discussed above, the electron density anomalies as revealed by 3-D tomography (Figures 5 and 8) only reflect the electron redistribution, and the net current would depend on the movements of positive ions. We drew Figure 11 assuming an arbitrary current, to let 4.5×10^{26} electrons (~0.15 of the amount in Figure 7b) flow along a thin line extending from the center of positive electron density anomaly at 330 km altitude upward along the magnetic field to 600 km altitude in 40 min. Then the Bio-Savard's law predicts the eastward field of ~3 nT in the Kanto District (Figure 11). This nearly coincides with the change in declination observed at the Kakioka observatory in Kanto (relative to Kanoya in Kyushu) starting ~40 min before the earthquake as reported in Figure 4 of Heki and Enomoto (2013). Anyway, the assumption is arbitrary (we do not have a theoretical basis for the value 0.15), and Figures 10 and 11 just provide a rough sketch illustrating how the induced polarization occurs.

We also assumed that the declination change at Kakioka (Heki & Enomoto, 2013) was not a regular space weather phenomenon. It should be born in mind, however, that the 2011 Tohoku-oki earthquake occurred during a magnetic storm. So we need a careful study to attribute the observed declination changes to the ionospheric electron redistribution process as proposed in this study. It would be also important to detect magnetic field changes immediately before many large earthquakes to draw a more realistic picture of the whole process.

6. Conclusions

We studied the 3-D structure of the ionospheric electron density anomalies immediately before the 2011 Tohoku-oki (M_w9.0) earthquake by using GNSS-TEC data taken in Japan and South Korea as the input to a 3-D tomography program. The linear inversion is stabilized by continuity and altitude-dependent constraints, and the performance of the method was confirmed by trying 3-D tomography to artificial patterns. The recovered electron density anomalies showed similar 3-D structure to the earlier study on the 2015 Chilean earthquake (He & Heki, 2018), that is, a low positive anomaly and a high negative electron density anomaly along the geomagnetic field. These anomalies lie above the land area rather than the offshore epicenter, suggesting surface charges responsible for the anomaly. The amount of the positive and the negative anomalies are nearly balanced suggesting that the anomalies were made by electron transport. We also studied the 3-D structure of the postseismic anomalies and found that the negative electron density anomaly emerged offshore just above the submarine fault. Variety of TEC change patterns observed before and after the 2011 Tohoku-oki earthquake is understood by different combinations of the penetrations of LoS with such electron density anomalies. Based on these results, we proposed a simple model emphasizing the electron redistribution by the induced polarization to cancel crust-origin electric field along the geomagnetic field.

Data Availability Statement

GIM for estimating the interfrequency bias for the Korean stations were downloaded online (aiub.unibe.ch/CODE). Fortran source codes used in this study can be downloaded online (www.ep.sci.hokudai.ac.jp/~heki/software.htm).

Acknowledgments
We thank the Geospatial Information Authority (GSI) for GEONET data (terras.gsi.go.jp) and Electric Navigation Research Institute (ENRI) for the interfrequency bias data for GEONET stations (www.enri.go.jp) and B.-K. Choi for Korean data (gnss.ngii.go.kr). We thank He Liming, Northeast University, for helpful comments, and Chihiro Yamanaka, Osaka University, for discussion on physical models. Constructive comments by two anonymous referees improved the quality of the paper.

References

Astafyeva, E., Lognonné, P., & Rolland, L. (2011). First ionospheric images of the seismic fault slip on the example of the Tohoku-oki earthquake. *Geophysical Research Letters*, *38*, L22104. https://doi.org/10.1029/2011GL049623

Astafyeva, E., & Shults, K. (2019). Ionospheric GNSS imagery of seismic source: Possibilities, difficulties, and challenges. *Journal of Geophysical Research: Space Physics*, *124*, 534–543. https://doi.org/10.1029/2018JA026107

Cahyadi, M. N., & Heki, K. (2015). Coseismic ionospheric disturbance of the large strike-slip earthquakes in North Sumatra in 2012: Mw dependence of the disturbance amplitudes. *Geophysical Journal International*, *200*(1), 116–129. https://doi.org/10.1093/gji/ggu343

Calais, E., & Minster, J. B. (1995). GPS detection of ionospheric perturbations following the January 17, 1994, Northridge earthquake. *Geophysical Research Letters*, *22*(9), 1045–1048. https://doi.org/10.1029/95GL00168

Choi, B.-K., & Hong, J. (2019). Observation of the fast-traveling ionospheric disturbances induced by the 2017 North Korean missile. *Advances in Space Research*, *63*(8), 2598–2608. https://doi.org/10.1016/j.asr.2018.12.033

Coster, A., Williams, J., Weatherwax, A., Rideout, W., & Herne, D. (2013). Accuracy of GPS total electron content: GPS receiver bias temperature dependence. *Radio Science*, *48*, 190–196. https://doi.org/10.1002/rds.20011

Freund, F. (2013). Earthquake forewarning—A multidisciplinary challenge from the ground up to space. *Acta Geophysica*, *61*(4), 775–807. https://doi.org/10.2478/s11600-013-0130-4

Freund, F. T. (2011). Pre-earthquake signals: Underlying physical processes. *Journal of Asian Earth Sciences*, *41*(4–5), 383–400. https://doi.org/10.1016/j.jseaes.2010.03.009

He, L., & Heki, K. (2016). Three-dimensional distribution of ionospheric anomalies prior to three large earthquakes in Chile. *Geophysical Research Letters*, *43*, 7287–7293. https://doi.org/10.1002/2016GL069863

He, L., & Heki, K. (2017). Ionospheric anomalies immediately before M_w7.0–8.0 earthquakes. *Journal of Geophysical Research: Space Physics*, *122*, 8659–8678. https://doi.org/10.1002/2017JA024012

He, L., & Heki, K. (2018). Three-dimensional tomography of ionospheric anomalies immediately before the 2015 Illapel earthquake, Central Chile. *Journal of Geophysical Research: Space Physics*, *123*, 4015–4025. https://doi.org/10.1029/2017JA024871

He, L., Heki, K., & Wu, L. (2018). Three-dimensional and trans-hemispheric ionospheric electron density changes by the great solar eclipse in North America on 21 August 2017. *Geophysical Research Letters*, *45*, 10,933–10,940. https://doi.org/10.1029/2018GL080365

Heki, K. (2011). Ionospheric electron enhancement preceding the 2011 Tohoku-oki earthquake. *Geophysical Research Letters*, *38*, L17312. https://doi.org/10.1029/2011GL047908

Heki, K. (2020). Chapter 5-3: Ionospheric disturbances related to earthquakes. In C. Huang & G. Lu (Eds.), *Advances in ionospheric research: Current understanding and challenges* (Vol. 3, pp. 1–320).

Heki, K., & Enomoto, Y. (2013). Preseismic ionospheric electron enhancements revisited. *Journal of Geophysical Research*, *118*, 6618–6626. https://doi.org/10.1002/jgra.50578

Heki, K., & Enomoto, Y. (2014). Reply to comment by K. Heki and Y. Enomoto on "Preseismic ionospheric electron enhancements revisited". *Journal of Geophysical Research: Space Physics*, *119*, 6016–6018. https://doi.org/10.1002/2014JA020223

Heki, K., & Enomoto, Y. (2015). M_w dependence of the preseismic ionospheric electron enhancements. *Journal of Geophysical Research: Space Physics*, *120*, 7006–7020. https://doi.org/10.1002/2015JA021353

Heki, K., & Ping, J.-S. (2005). Directivity and apparent velocity of the coseismic ionospheric disturbances observed with a dense GPS array. *Earth and Planetary Science Letters*, *236*(3-4), 845–855. https://doi.org/10.1016/j.epsl.2005.06.010

Inchin, P. A., Snively, J. B., Williamson, A., Melgar, D., Aguilar Guerrero, J., & Zettergren, M. D. (2020). Mesopause airglow disturbances driven by non-linear infrasonic acoustic waves generated by large earthquakes. *Journal of Geophysical Research: Space Physics*, *125*, e2019JA027628. https://doi.org/10.1029/2019JA027628

Iwata, T., & Umeno, K. (2016). Correlation analysis forpreseismic total electron content anomalies around the 2011 Tohoku-oki earthquake. *Journal of Geophysical Research: Space Physics*, *121*, 8969–8984. https://doi.org/10.1002/2016JA023036

Kakinami, Y., Kamogawa, M., Tanioka, Y., Watanabe, S., Gusman, A. R., Liu, J.-Y., et al. (2012). Tsunamigenic ionospheric hole. *Geophysical Research Letters*, *39*, L00G27. https://doi.org/10.1029/2011GL050159

Kamogawa, M., & Kakinami, Y. (2013). Is an ionospheric electron enhancement preceding the 2011 Tohoku-oki earthquake a precursor? *Journal of Geophysical Research: Space Physics*, *118*, 1751–1754. https://doi.org/10.1002/jgra.50118

Kelley, M. C., Swartz, W. E., & Heki, K. (2017). Apparent ionospheric total electron content variations prior to major earthquakes due to electric fields created by tectonic stresses. *Journal of Geophysical Research: Space Physics*, *122*, 6689–6695. https://doi.org/10.1002/2016JA023601

Kuo, C. L., Lee, L. C., & Huba, J. D. (2014). An improved coupling model for the lithosphere- atmosphere-ionosphere system. *Journal of Geophysical Research: Space Physics*, *119*, 3189–3205. https://doi.org/10.1002/2013JA019392

Masci, F., Thomas, J., Villani, F., Secan, J., & Rivera, N. (2015). On the onset of ionospheric precursors 40 min before strong earthquakes. *Journal of Geophysical Research: Space Physics*, *120*, 1383–1393. https://doi.org/10.1002/2014JA020822

Muafiry, I. N., Heki, K., & Maeda, J. (2018). 3D tomography of midlatitude sporadic-E in Japan from GNSS-TEC data. *Earth, Planets and Space*, *70*(1). https://doi.org/10.1186/s40623-018-0815-7

Ozawa, S., Nishimura, T., Suito, H., Kobayashi, T., Tobita, M., & Imakiire, T. (2011). Coseismic and postseismic slip of the 2011 magnitude-9 Tohoku-Oki earthquake. *Nature*, *475*(7356), 373–376. https://doi.org/10.1038/nature10227

Rideout, W., & Coster, A. (2006). Automated GPS processing for global total electron content data. *GPS Solutions*, *10*(3), 219–228. https://doi.org/10.1007/s10291-006-0029-5

Rolland, L. M., Vergnolle, M., Nocquet, J.-M., Sladen, A., Dessa, J.-X., Tavakoli, F., et al. (2013). Discriminating the tectonic and non-tectonic contributions in the ionospheric signature of the 2011, M_w7.1, dip-slip Van earthquake, Eastern Turkey. *Geophysical Research Letters*, *40*, 2518–2522. https://doi.org/10.1002/grl.50544

Sakai, T. (2005). *Bias error calibrations for observing ionosphere by GPS network* (Vol. J88-B, pp. 2382–2389). Japan: The Instutite of Electronics, Information and Communication Engineers.

Shinagawa, H., Tsugawa, T., Matsumura, M., Iyemori, T., Saito, A., Maruyama, T., et al. (2013). Two-dimensional simulation of ionospheric variations in the vicinity of the epicenter of the Tohoku-oki earthquake on 11 March 2011. *Geophysical Research Letters*, *40*, 5009–5013. https://doi.org/10.1002/2013GL05762

Utada, H., & Shimizu, H. (2014). Comment on "Preseismic ionospheric electron enhancements revisited" by K. Heki and Y. Enomoto. *Journal of Geophysical Research: Space Physics*, *119*, 6011–6015. https://doi.org/10.1002/2014JA020044

Zettergren, M. D., & Snively, J. B. (2019). Latitude and longitude dependence of ionospheric TEC and magnetic perturbations from infrasonic-acoustic waves generated by strong seismic events. *Geophysical Research Letters*, *46*, 1132–1140. https://doi.org/10.1029/2018GL081569